April 2026
Volume 2
Issue 2

Interdisciplinary Journal of Civil Engineering
Shahid Beheshti University

DOI: 10.48308/ijce.2026.246017.1028

Investigating the Role of Caspian Sea-Level Decline in Intensifying Surface Urban Heat Islands in the Coastal Cities of Northern Iran

Authors:

Seyyed Ehsan Abbasi [1], Saeid Sadeghian [1, *]

Abstract

Urban expansion and replacing natural land with impervious surfaces drive (UHI[2]) formation. Along northern Iran, this phenomenon is influenced by urban development, hydrological fluctuations, and the Caspian Sea's declining water level, which weakens its climatic moderating effect. This study examined ten-year changes in (LST[3]) and Caspian Sea water extent (2015–2025) across Gilan, Mazandaran, and Golestan provinces. The framework relied on cloud computing and processing Landsat 8/9 imagery in GEE[4]. Water bodies were delineated using the (MNDWI[5]), while LST was retrieved from Landsat thermal bands. Satellite-derived temperatures were validated against NASA POWER data. Linear regression showed strong agreement (R^2 of 0.8376, 0.8699, and 0.8830 for Rasht, Sari, and Gorgan). Findings revealed a complex link between water extent shifts and thermal behavior. The most pronounced water retreat occurred in 2022, exposing barren coastal land and intensifying thermal hotspots. An exceptional thermal peak of 30.8 °C in 2021 potentially heightened evaporation and subsequent water retreat. Interprovincial comparisons demonstrated that Golestan experienced higher surface temperatures than Mazandaran and Gilan due to its drier climate and more pronounced shoreline retreat. Overall, Caspian Sea hydrological changes significantly drive thermal instability along northern Iran's coast. Consequently, sustainable planning for coastal cities must integrate sea-level decline scenarios and climate-adaptation strategies.

1. Department of Geoinformation and Geomatics Engineering, Faculty of Civil, Water and Environmental Engineering, Shahid Beheshti University, Tehran, Iran

*Corresponding Author: sa_sadeghian@sbu.ac.ir

2. Urban Heat Island

3. Land Surface Temperature

4. Google Earth Engine

5. Modified Normalized Difference Water Index

Keywords: Urban Heat Island, Caspian Sea, Land Surface Temperature, Google Earth Engine, Remote Sensing

1. Introduction

The (UHI) effect is among the most evident environmental consequences of rapid urbanization. It is generally characterized by a significant temperature difference between densely developed urban areas and their surrounding suburban or rural environments (Nadeem & others, 2023). The expansion of built-up surfaces, loss of vegetation, alteration of surface radiative properties, and increase in anthropogenic heat emissions modify the urban energy balance and contribute to rising temperatures.

Over recent decades, scientific interest in identifying the drivers of UHIs and developing effective mitigation measures has increased considerably. Bibliometric assessments indicate that, between 1991 and 2015, research gradually shifted from limited station-based observations toward remote sensing, field measurements, and spatial analysis (Huang & Lu, 2018). Today, the integration of satellite imagery with advanced models and microscale simulations enables a more detailed understanding of urban thermal dynamics and supports the evaluation of adaptation measures, including cooling systems and green infrastructure (Sayah et al., 2023).

The significance of the UHI effect extends beyond the direct warming of urban environments. Higher temperatures increase the demand for building cooling and, consequently, energy consumption and carbon emissions (Dwivedi & Soni, 2024). At the same time, extreme urban heat can degrade air quality and intensify health risks, including heat-related mortality (Macintyre et al., 2021). Identifying the spatial and temporal patterns of UHIs has therefore become an important research priority in urban climatology, spatial planning, and energy management (Wong et al., 2021).

The northern coastal zone of Iran presents a particularly complex setting. In addition to the expansion of impervious surfaces and urban centers, the provinces of Gilan, Mazandaran, and Golestan are affected by hydrological fluctuations in the Caspian Sea. Historically, this large water body has played an important role in regulating local climatic conditions through its thermal inertia and the circulation of sea breezes. However, the decline in water level and the associated shoreline retreat observed in recent years may have altered the extent and effectiveness of this moderating function (Caspian Sea Studies & Center, 2025).

As the sea retreats, sections of its former bed are exposed and transformed into barren land with little or no vegetation. Compared with a water surface, such areas have a greater potential to absorb solar energy and develop high surface temperatures. They may consequently generate new thermal hotspots and intensify regional land surface warming (Fu & Weng, 2016). Therefore, investigating urban heat in the coastal cities of northern Iran without considering shoreline dynamics and changes in water extent may provide an incomplete account of the processes governing the region's thermal conditions.

Landsat imagery offers an appropriate basis for the simultaneous monitoring of water-body changes and LST because of its suitable spatial resolution, long historical record, and availability of thermal bands. These characteristics make it possible to investigate the relationship between shoreline retreat and regional thermal dynamics across both space and time (Fu & Weng, 2016). Accordingly, this study employs Landsat 8 and 9 imagery and the cloud-computing capabilities of GEE to analyze changes in LST and the extent of the Caspian Sea over a ten-year period. It further seeks to clarify the potential role of water retreat in intensifying surface warming across the coastal cities of northern Iran.

2. Literature Review

2.1. Evolution of Approaches to UHI Monitoring

Methods used to investigate UHIs have evolved substantially over recent decades. Bibliometric studies indicate that, since the beginning of the 1990s, researchers have become less dependent on sparse meteorological station observations and increasingly adopted remote-sensing technologies and numerical modeling (Huang & Lu, 2018). This methodological transition has enabled the observation of thermal patterns over extensive areas and the simultaneous comparison of different sections of a city.

Advances in thermal sensors and the development of modeling methods across local and regional scales have also improved the identification of critical thermal hotspots within complex urban landscapes (Sayah et al., 2023). Time-series satellite imagery, particularly the Landsat archive, allows long-term LST dynamics to be examined in relation to urban growth, vegetation change, and land-use transformation (Fu & Weng, 2016). Consequently, recent research has progressed beyond simply describing urban–rural temperature differences and now gives greater attention to the spatial, temporal, and environmental processes underlying UHI formation.

2.2. Physical Drivers and Environmental Consequences

A substantial body of research identifies urbanization and the associated modification of land-surface properties as the principal causes of urban thermal anomalies (Nadeem & others, 2023). The replacement of soil and vegetation with concrete, asphalt, and other construction materials reduces surface permeability and increases heat-storage capacity. At the same time, reduced evapotranspiration and restricted airflow within compact urban structures intensify heat accumulation.

The effects of increasing urban temperatures extend across several interconnected domains. Greater dependence on mechanical cooling increases building energy consumption and carbon emissions, which can further reinforce local warming (Dwivedi & Soni, 2024; Feinberg, 2023). Previous studies have also reported associations between high temperatures, elevated concentrations of certain atmospheric pollutants, and increased health risks during periods of extreme heat. These conditions can threaten public health and raise the rate of heat-related mortality (Macintyre et al., 2021).

2.3. Mitigation Strategies and the Challenges of Coastal Environments

A broad range of adaptation and mitigation measures has been proposed in response to increasing urban thermal risks. Green infrastructure, improved connectivity between vegetated areas, the use of high-albedo materials, and spatially optimized urban design are among the principal approaches proposed for reducing urban temperatures and supporting sustainable urban development (Wong et al., 2021).

Nevertheless, the thermal behavior of coastal cities is not determined solely by their physical structure. In coastal environments, sea level, shoreline position, local breezes, and the thermal properties of adjacent water bodies are also important. Shoreline retreat may increase the distance between urban areas and the water body, thereby reducing the sea's cooling influence. Simultaneously, the exposure of barren land may increase solar-energy absorption and create favorable conditions for the emergence of new thermal anomalies (Caspian Sea Studies & Center, 2025). UHI analysis in coastal cities should therefore adopt an integrated approach that considers interactions between urban development and hydrological processes.

2.4. Analytical Review of Recent Studies, 2019–2026

Recent literature demonstrates that research on LST, UHIs, and water-body dynamics has increasingly adopted advanced spatial-statistical algorithms, predictive modeling, and multiclimate analysis. To provide a coherent account of these developments, previous studies can be organized into four principal themes.

2.4.1. Thermal Dynamics and Water-Level Fluctuations in the Caspian Sea Basin

Climatic and hydrological changes in the Caspian Sea have attracted growing scientific attention. (Beyraghdar Kashkooli et al., 2019) analyzed a 35-year satellite dataset covering 1982–2016 and found that the rate of sea-surface warming in the southern Caspian Sea was higher than the mean warming rate of the world's oceans. Their results also indicated an increasing trend in annual maximum sea-surface temperature, particularly in offshore areas, together with a significant extension of the warm season.

(Azizpour & Ghaffari, 2022) applied cross-wavelet analysis to examine low-frequency and seasonal variations in the Caspian Sea level. Their findings suggested that increasing evaporation over the central basin, combined with fluctuations in the discharge of the Volga River and a time lag of one to two months, influenced changes in water level. They also highlighted the contribution of large-scale atmospheric circulation patterns, including the negative phases of the Arctic Oscillation and North Atlantic Oscillation, to the pronounced decline in the Caspian Sea level since the 1990s.

Despite the value of these studies, direct linkages between marine hydrodynamic models and the thermal characteristics of coastal terrestrial environments remain insufficiently investigated. In particular, the simultaneous effects of shoreline retreat on land-surface thermal anomalies in adjacent areas require more comprehensive analysis.

2.4.2. Methodological Innovations in Spatiotemporal Urban Heat Analysis

The development of statistical indices that evaluate the spatial and temporal dimensions of UHIs simultaneously represents an important methodological advancement. (Weng et al., 2019) used Pearson's chi-square test and Shannon entropy and introduced the Degree-of-Goodness index to examine unstable and asymmetric patterns of surface UHI intensity in different geographical directions across Babol. Their results demonstrated that variations in thermal conditions were associated with the expansion of built-up land and population growth.

(Ghanghermeh et al., 2024) integrated (EHSA[1]) with the nonparametric Mann–Kendall test to identify complex thermal-anomaly patterns in the humid subtropical climate of Sari. Their findings showed that although vegetation expansion contributed to thermal moderation in some areas, the overall trajectory of climatic change promoted increasingly uniform warm conditions in the city center

A shared limitation of these investigations is their emphasis on intra-urban areas, with limited consideration of the transitional land–sea zone. Furthermore, classification systems based on (LCZ[2]s) have not yet been used sufficiently in fine-scale regional studies.

2.4.3. Landscape Structure, Connectivity, and Climatic Variatio

The response of LST to land-use change is not uniform across climatic regions. (Karimi Firozjaei et al., 2025) used a Cellular Automata–Markov Chain model to predict daytime surface UHI intensity through 2058 under five climatic regimes in Iran. Their findings showed that the response of LST was strongly influenced by the background climate and the pattern of urban physical development. In humid cities such as Rasht and Babol, the expansion of built-

[1] Emerging Hot Spot Analysis
[2] Local Climate Zones

up surfaces intensified the UHI effect. In contrast, in arid and semi-arid cities such as Mashhad and Yazd, the thermal influence of surrounding barren land was more pronounced.

From the perspective of green-space connectivity, (Omidighalehmohammadi et al., 2026) applied circuit theory in Tehran and found that the fragmentation of green spaces and expansion of dry patches reduced the ability of vegetation to moderate temperature and disrupted the cooling performance of urban green networks.

At the international scale, (Zhao et al., 2026) examined coastal cities worldwide within an LCZ framework. They demonstrated that temperature intensity across coastal zones was jointly regulated by the cooling influence of the ocean and the density of built-up land. Their findings further suggested that the cooling effectiveness of vegetation, measured using the (NDVI[3]), changed with increasing distance from the coast. Studies conducted by (Hedeya et al., 2025) in Montreal and (Ojerinde et al., 2026) in Nigerian cities similarly emphasized the roles of vegetation degradation and compact urban form in pushing thermal-comfort indices beyond critical thresholds during heatwaves.

2.4.4. Urban Resilience and Nature-Based Responses to Climate Change

Within the fields of disaster management and climate foresight, (Liang et al., 2026) modeled the resilience of Shanghai’s urban districts to sea-level rise and coastal flooding through 2100. Their results showed a substantial decline in resilience indicators under business-as-usual scenarios. Accordingly, they proposed a transition toward nature-based solutions and blue–green infrastructure as a sustainable pathway for reducing climate-related risks.

Although this category of research has mainly focused on sea-level rise, its conceptual framework is also relevant to regions experiencing declining water levels. Under both conditions, the displacement of the shoreline can transform ecological structures, local thermal conditions, and the vulnerability of coastal settlements. Urban adaptation strategies should therefore reflect the direction and magnitude of local shoreline change rather than applying a uniform solution to all coastal environments.

2.5. Synthesis of Previous Research and the Novelty of the Present Study

A synthesis of the literature indicates that, despite substantial progress in research on LST and UHIs, several important gaps remain.

First, hydrological studies of the Caspian Sea, such as (Azizpour & Ghaffari, 2022), have primarily focused on the factors governing water-level fluctuations. By contrast, LST studies, including (Ghanghermeh et al., 2024), have generally examined urban thermal behavior independently. Few studies have simultaneously modeled shoreline retreat, the weakening of

[3] Normalized Difference Vegetation Index

the thermal moderation provided by the water body, and the formation of warmer barren surfaces.

Second, many regional investigations have relied on single-date imagery or relatively short observation periods. Although such datasets may capture seasonal conditions, they are insufficient for distinguishing temporary fluctuations from persistent climatic trends. The present study uses the cloud-computing capabilities of GEE and a Landsat time series to examine annual and long-term changes in both thermal and hydrological variables. This approach enables persistent temperature anomalies and the gradual consequences of shoreline retreat to be identified with greater confidence.

Third, the validation of remotely sensed temperature estimates using independent atmospheric datasets has received limited attention in previous research. In this study, satellite-derived temperature estimates are compared with NASA POWER reanalysis data. This step makes it possible to assess the temporal consistency of the results and improves confidence in their thermal interpretation.

The principal contribution of the present study therefore lies in integrating three components:

long-term analysis of changes in the Caspian Sea's water extent, simultaneous monitoring of LST across three coastal provinces, and validation of satellite-derived results using an independent climatic dataset. This integrated framework can provide a more comprehensive understanding of the relationships among sea-level decline, the exposure of coastal land, and the intensification of surface thermal anomalies in northern Iran.

3. Materials and Methods

The methodological framework of this study was designed as a sequential, structured, and reproducible workflow that enabled the simultaneous monitoring and integrated analysis of hydrological and thermodynamic changes along the Caspian Sea coastline. To ensure methodological transparency and consistency with the conceptual framework, the study was implemented through eight principal stages, as illustrated in Figure 1.

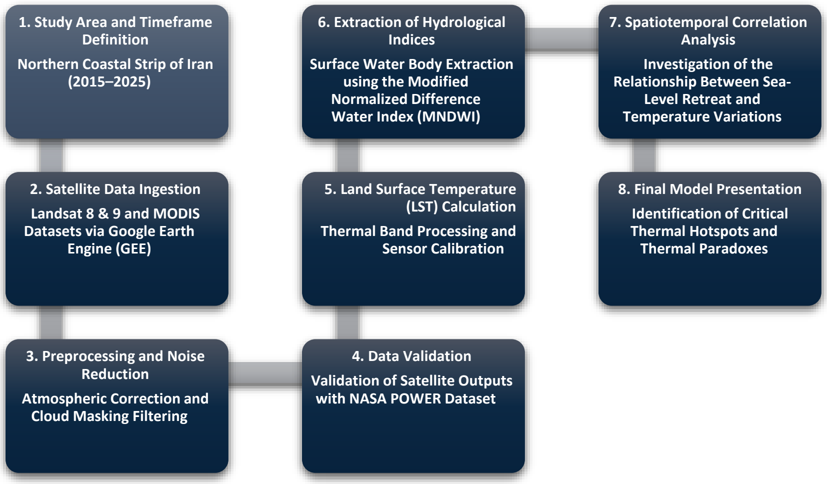

Figure 1. Main stages of the research workflow (Source: Research findings, 2026)

3.1. Definition of the Study Area and Temporal Period

The study area encompasses the northern coastal zone of Iran, administratively comprising the provinces of Gilan, Mazandaran, and Golestan. Located along the southern coast of the Caspian Sea, the world's largest enclosed inland water body, this region exhibits considerable climatic diversity. Climatic conditions range from humid Mediterranean-type conditions in western Gilan to semi-arid and steppe environments in eastern Golestan.

The coexistence of climate-sensitive ecosystems, densely populated urban centers, and extensive agricultural land makes this region particularly suitable for investigating interactions between hydrological change and surface thermal dynamics. In addition to the urban and built-up areas of the provincial capitals, Rasht, Sari, and Gorgan. The entire water extent of the Caspian Sea within the territorial boundary of the Islamic Republic of Iran was incorporated into the analytical framework.

The study period extended from January 2015 to December 2025. This long-term temporal coverage made it possible to move beyond short-term seasonal variability and examine broader climatic trends, persistent thermal anomalies, and the lasting effects of shoreline retreat on coastal microclimates in Figure 2.

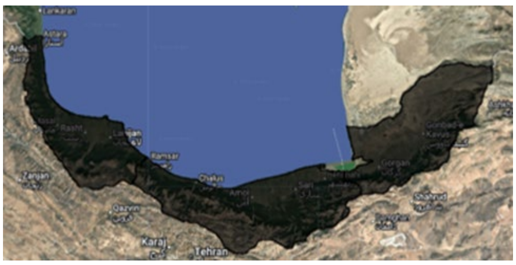

Figure 2. Location of the study area (Source: Research findings, 2026).

3.2. Retrieval of Satellite Data

The extensive spatial coverage of the study area and the large volume of imagery required for a multiyear analysis made conventional image-processing workflows based on the physical downloading of satellite scenes inefficient. (GEE) was therefore used as the principal cloud-computing environment. This platform provides direct access to global remote-sensing archives and supports large-scale geospatial processing (Gorelick et al., 2017).

The principal geometric and spectral datasets were obtained from the (USGS[4]) archive (U.S. Geological Survey, 2024). These datasets included Landsat 8 imagery acquired by the Operational Land Imager and Thermal Infrared Sensor (OLI/TIRS), as well as Landsat 9 imagery acquired by the OLI-2 and TIRS-2 sensors. Landsat Collection 2, Level 2, Tier 1 products were used throughout the study (U.S. Geological Survey, 2024).

These products are supplied with geometric and orthorectification corrections already applied. Landsat imagery, with a spatial resolution of 30 m for the principal multispectral bands, constituted the primary data source for calculating the hydrological and vegetation indices.

In addition, the MODIS land surface temperature product MOD11A2 was incorporated into the GEE database to support the monitoring of diurnal thermal behavior and broader temporal analyses.

3.3. Preprocessing and Noise Removal

Although Landsat Collection 2 Level 2 products provide atmospherically corrected surface-reflectance and surface-temperature values, additional quality-control procedures were necessary to ensure the reliability and temporal consistency of the results.

A dynamic cloud mask was therefore developed and applied to all images using the Landsat quality-assurance band. Pixels affected by cloud cover, cloud shadow, and heavy atmospheric haze were excluded from further calculations.

As an initial filtering criterion, only scenes with total cloud cover below 15% were included in the processing workflow. Because solar illumination geometry varies across seasons, topographic correction functions and solar-azimuth corrections were also applied. These procedures improved spectral consistency across the 2015–2025 image series and reduced the likelihood that atmospheric contamination or variations in illumination geometry would introduce false anomalies into the final model (U.S. Geological Survey, 2024).

3.4. Extraction of Hydrological Indices

[4] United States Geological Survey

The hydrological component of the study was based on the (MNDWI), which was used to monitor the dynamic behavior of the Caspian Sea shoreline accurately (Xu, 2006). Unlike the conventional Normalized Difference Water Index, MNDWI uses the shortwave infrared band instead of the near-infrared band.

The index was calculated as follows:

$$MNDWI = \frac{Green - SWIR}{Green + SWIR}$$

(1)

For Landsat 8 and 9 imagery, Band 3 (Green) and Band 6 (SWIR-1) were used as the inputs to Equation 1. The effectiveness of MNDWI stems from the strong reflectance of built-up surfaces in the SWIR region compared with their reflectance in the green band. Water, by contrast, produces a distinctly different spectral response in these two bands. This property suppresses spectral noise associated with coastal urban structures and improves the separation of water and land boundaries at the 30-m spatial resolution of Landsat imagery.

An optimized threshold was applied to extract the annual water pixels of the Caspian Sea. Spatial differencing was subsequently performed between consecutive years, allowing coastal land to be classified into three stable categories: unchanged areas, areas affected by water retreat, and areas experiencing water advancement (Gorelick et al., 2017). This analysis enabled the area exposed by shoreline retreat to be quantified for each year.

3.5. Calculation of Land Surface Temperature

The thermodynamic component of the study focused on retrieving an accurate LST time series from Band 10 of the TIRS and TIRS-2 sensors aboard Landsat 8 and 9. The physical calculations were implemented in Google Earth Engine using a four-stage processing chain (Gorelick et al., 2017).

3.5.1. Calculation of Brightness Temperature

First, the raw digital numbers of Landsat Band 10 were converted to top-of-atmosphere spectral radiance $L_\lambda$using the rescaling coefficients provided in the image metadata. The spectral radiance was then converted to at-sensor brightness temperature T_B, expressed in kelvin, using the inverse Planck function (2):

$$T_B = \frac{K_2}{\ln\left(\frac{K_1}{L_\lambda} + 1\right)}$$

(2)

where K_1 and K_2 are the thermal-band calibration constants provided for the Landsat sensor.

3.5.2. Calculation of the Normalized Difference Vegetation Index

To estimate surface emissivity, the Normalized Difference Vegetation Index (NDVI) was first calculated using the near-infrared and red bands (3):

$$NDVI = \frac{NIR - Red}{NIR + Red}$$

(3)

NDVI was used to represent the density and spatial distribution of vegetation within the study area.

3.5.3. Estimation of Fractional Vegetation Cover-P_v

Fractional vegetation cover $\boldsymbol{P_v}$ was estimated using a minimum NDVI value of 0.2 for bare soil and a maximum NDVI value of 0.5 for dense vegetation. The fractional vegetation cover-P_v of each pixel was calculated as follows (4):

$$P_v = \left(\frac{NDVI - NDVI_{min}}{NDVI_{max} - NDVI_{min}}\right)^2$$

(4)

3.5.4. Estimation of Land Surface Emissivity- ε and Final LST Retrieval

Land surface emissivity ε , representing the thermal-emission capacity of soil and vegetation, was estimated from fractional vegetation cover using the following empirical relationship (5):

$$\varepsilon = 0.004 \cdot P_v + 0.986$$

(5)

Finally, brightness temperature T_B and surface emissivity ε were incorporated into the single-channel atmospheric-correction equation to derive actual LST in degrees Celsius (6):

$$LST\ (°C) = \left(\frac{T_B}{1 + \left(\frac{\lambda \cdot T_B}{\rho}\right) \cdot \ln(\varepsilon)}\right) - 273.15$$

(6)

where λ is the effective wavelength of the thermal band and ρ is a physical constant derived from Planck's constant, the Boltzmann constant, and the speed of light.

3.6. Data Validation

The northern coastal region of Iran is characterized by variable atmospheric conditions, including high humidity and seasonal fog, which may affect satellite thermal signals. Independent validation of the remotely sensed outputs was therefore necessary.

NASA POWER reanalysis data from global stations located near ground level were used for this purpose (NASA POWER Project, 2024). This database provides atmospheric and surface-temperature estimates derived through the integration of station observations and numerical weather-prediction models.

Daily and monthly temperature values derived from the Landsat processing workflow in GEE were extracted for pixels corresponding to the provincial capitals of Rasht, Sari, and Gorgan. These values were subsequently compared with temporally corresponding NASA POWER air-temperature data.

Validation was performed using statistical error indicators, including the (RMSE[5]), coefficient of determination R^2, and systematic bias. These measures were used to assess the agreement, accuracy, and consistency of the satellite-derived temperature estimates.

The validation results demonstrated strong statistical agreement between the two datasets. The coefficients of determination were 0.8376 for Rasht, 0.8699 for Sari, and 0.8830 for Gorgan. These high values supported the reliability of the calibration procedure and the effectiveness of cloud-based Landsat processing for regional thermal classification (Figure 3a,3b,3c).

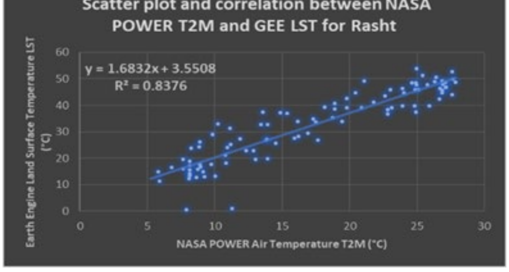

[5] Root Mean Square Error

Figure 3a. Scatterplot and relationship between NASA POWER 2-m air temperature and Google Earth Engine-derived LST at the Rasht station, 2015–2025(Source: Research findings, 2026).

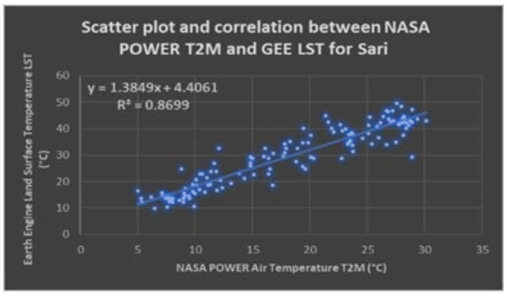

Figure 3b. Scatterplot and relationship between NASA POWER 2-m air temperature and Google Earth Engine-derived LST at the Sari station, 2015–2025(Source: Research findings, 2026).

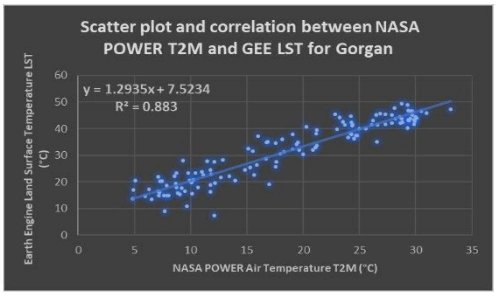

Figure 3c. Scatterplot and relationship between NASA POWER 2-m air temperature and Google Earth Engine-derived LST at the Gorgan station, 2015–2025(Source: Research findings, 2026).

3.7. Spatiotemporal Correlation Analysis

After constructing the hydrological database, represented by the Caspian Sea water extent derived from MNDWI, and the thermodynamic database, represented by the LST time series, the structural relationship between these two variables was examined.

Pearson's correlation analysis and spatial linear regression were applied to the raster layers. The principal objective was to determine how LST responded to changes in shoreline position. The analysis was conducted at two spatial scales.

At the regional scale, annual changes in the total water extent of the Caspian Sea were compared with mean LST across the coastal zone. This analysis was intended to identify shared anomalies and critical years, particularly 2021 and 2022.

At the local scale, the rate of temperature increase was examined specifically across land exposed by water retreat. This analysis was designed to determine the direct effect of vegetation removal and the exposure of barren soil on surface temperature.

3.8. Development of the Final Conceptual Model

In the final stage, the information layers were synthesized and integrated. Spatial correlation maps, persistent thermal hotspots, and the expansion of UHIs around the principal urban centers of Gilan, Mazandaran, and Golestan were overlaid, classified, and prioritized.

This synthesis led to the development of a conceptual water–thermal paradox model for the southern coast of the Caspian Sea. The model proposes that global warming first increases atmospheric temperature, after which intensified evaporation accelerates water retreat. The resulting reduction in sea-breeze cooling then promotes the stabilization and expansion of terrestrial thermal hotspots.

4. Results

4.1. Temporal Variation in the Caspian Sea Water Level, 2015–2025

Analysis of the GEE outputs revealed that the Caspian Sea's water extent followed a fluctuating but generally declining trajectory over the study period.

Annual monitoring showed that the greatest single-year reduction occurred in 2022, when the water-covered area decreased by 13,025.62 km² relative to the preceding year. This change represents a substantial shoreline retreat.

Although a temporary increase of 12,052.98 km² was recorded in 2020, the water body entered a persistent declining phase after 2022, and its extent continued to decrease through 2025. The continuing retreat observed between 2023 and 2025 exposed extensive coastal areas with little or no vegetation, creating surfaces potentially susceptible to intensified land-surface warming.

The annual changes in water extent were as follows (Table1):

Table1. Annual increase or decrease in the water extent of the Caspian Sea between 2015 and 2025(Source: Research findings, 2026)

2016 relative to 2015	increase of 5,701.62 km²
2017 relative to 2016	decrease of 7,467.62 km²
2018 relative to 2017	increase of 2,462.26 km²
2019 relative to 2018	decrease of 8,770.26 km²
2020 relative to 2019	increase of 12,052.98 km²
2021 relative to 2020	increase of 8,228.42 km²
2022 relative to 2021	decrease of 13,025.62 km²
2023 relative to 2022	decrease of 2,090.34 km²
2024 relative to 2023	decrease of 609.58 km²
2025 relative to 2024	decrease of 1,848.17 km²

4.2. Relationship Between Water-Extent Change and Land Surface Temperature

The comparative analysis of water extent and LST confirmed a meaningful interaction between the two variables. A notable thermal peak occurred in 2021, when the regional mean LST exceeded 30. 8°C.The timing of this event is particularly important because the most substantial reduction in water extent occurred in the following year, 2022. The observed pattern suggests that the exceptionally high temperatures of 2021 may have intensified evaporation and contributed to the subsequent decline in water extent. As the water-covered area decreased, the thermal-moderation capacity of the Caspian Sea was also reduced. This loss of cooling influence coincided with abrupt increases in surface temperature across coastal areas, particularly where water retreat exposed barren land (Figure 4).

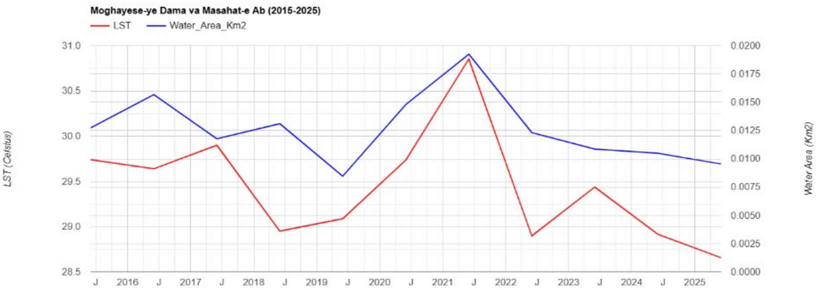

Figure 4. Comparative variation in Caspian Sea water extent and land surface temperature (Source: Research findings, 2026)

The spatial pattern for 2022 further showed that areas of water loss were closely associated with newly exposed coastal surfaces. These locations displayed elevated thermal conditions compared with adjacent water-covered areas, supporting the hypothesis that shoreline retreat contributes to the formation and expansion of coastal thermal hotspots (Figure 5).

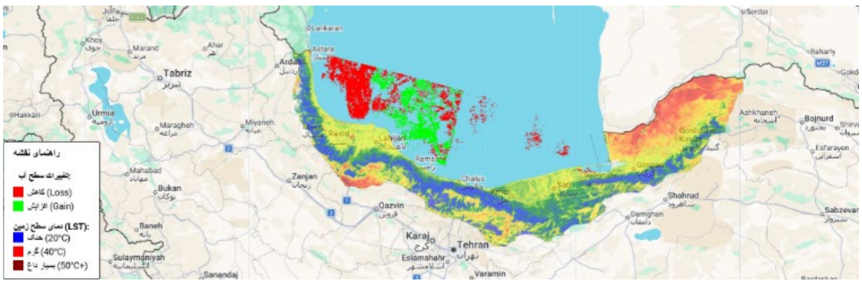

Figure 5. Spatial distribution of land surface temperature and water extent in 2022(Source: Research findings, 2026)

4.3. Comparative Analysis of Annual Temperature Dynamics across Guilan, Mazandaran, and Golestan Provinces

derived from ground station validation and satellite monitoring reveals that Golestan Province has systematically experienced significantly higher temperatures than the other two provinces (Table 2).

Table 2. Annual Mean Temperature of the Three Coastal Provinces of Iran (NASA POWER Project, 2024)

YEAR	GOLESTAN	MAZANDARAN	GILAN
2015	13.5	6.21	5.7
2016	13.48	6.32	5.59
2017	13.89	6.33	5.73
2018	13.38	6.16	5.55
2019	12.95	5.98	5.55
2020	13.26	6.05	5.42
2021	14.12	6.52	6.07
2022	13.66	6.42	5.7
2023	14	6.74	5.83
2024	13.39	6.26	5.33
2025	13.77	6.4	5.68

As detailed in Table 2, the mean annual temperature of Golestan Province over the 11-year study period (2015–2025) consistently hovered between 12.95 °C and 14.12 °C. In contrast, the mean annual temperature fluctuated between 5.98 °C and 6.74 °C in Mazandaran Province and between 5.33 °C and 6.07 °C in Guilan Province. This thermal disparity demonstrates a distinct east-to-west gradient in the thermal behavior of the southern Caspian Sea coastal strip.

A temporal trends analysis of the data reveals several key structural patterns. First, Golestan consistently maintained a thermal dominance throughout all study years, recording a mean temperature more than double that of Mazandaran and Guilan. For example, during 2021, one of the warmest years in this 11-year span, Golestan's mean temperature reached 14.12 °C, compared to 6.52 °C in Mazandaran and 6.07 °C in Guilan.

Second, thermal peaks and troughs occurred synchronously across all three provinces, following a unified macro-climatic fluctuation pattern. The year 2019 recorded the lowest temperatures across all regions (Golestan: 12.95 °C, Mazandaran: 5.98 °C, Guilan: 5.55 °C), whereas 2021 and 2023 marked regional thermal peaks, with Mazandaran experiencing its highest annual mean temperature of 6.74 °C in 2023.

Third, geographic features and land cover configurations heavily influenced these spatial discrepancies. The substantial temperature elevation in Golestan relative to the western provinces can be attributed to several environmental drivers: its geographical proximity to the arid and semi-arid zones east of the Caspian Sea and Turkmenistan's deserts, unlike Guilan and Mazandaran, which benefit more directly from the humidifying and moderating effects of the Caspian Sea; the greater density of Hyrcanian forests in Guilan and Mazandaran, which significantly mitigates (LST) through evapotranspiration; and a precipitation gradient that declines from west (Guilan) to east (Golestan), resulting in lower soil moisture and consequently higher surface thermal emissivity in Golestan.

Overall, ground-based and satellite validation results confirm that Golestan Province exhibits the most severe thermal conditions along northern Iran's coastal strip. Consequently, any strategic climate risk management, heatwave vulnerability planning, or future LST forecasting must give primary focus to this province while accounting for regional patterns. Specifically, Golestan's mean temperature continuously fluctuated between 12.95 °C and 14.12 °C, reaching its peak in 2021 (Figure 6).

Figure 6. Annual Temperature Trend of Golestan Province (NASA POWER Project, 2024)

Mazandaran displayed a mid-range trajectory with a mean temperature of approximately 6.4 °C in 2025, reflecting a modest increase compared to 2015 (Figure 7).

Figure 7. Annual Temperature Trend of Mazandaran Province (NASA POWER Project, 2024)

Meanwhile, Guilan maintained the lowest overall temperature range (5.33 °C to 6.07 °C), yet exhibited synchronous fluctuations with the other provinces during critical climate years such as 2021 (Figure 8).

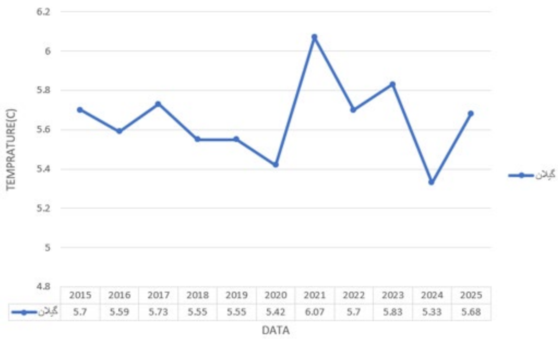

Figure 8. Annual Temperature Trend of Guilan Province (NASA POWER Project, 2024)

These inter-provincial contrasts demonstrate that the eastern Caspian region (Golestan), driven by drier climatic conditions and more pronounced sea-level retreat, faces a heightened vulnerability to surface urban heat island intensification.

5. Discussion and Overall Conclusions

This study investigated the relationship between changes in the water extent of the Caspian Sea and (LST) along the northern coast of Iran during 2015–2025. The findings reveal that the region's thermal dynamics are shaped by the combined influence of shoreline retreat, climatic variability, vegetation conditions, and urban development. Although the relationship between water extent and LST was not uniform across all years, the results suggest that the continued contraction of the Caspian Sea may increase the thermal vulnerability of adjacent coastal areas by exposing barren surfaces and weakening the moderating influence of the water body.

The most pronounced reduction in the mapped water extent occurred in 2022, following the exceptional thermal peak observed in 2021. This temporal sequence may indicate a delayed hydrological response to atmospheric and surface warming. Elevated temperatures can increase evaporation and contribute to subsequent reductions in water extent, although water-level fluctuations in the Caspian Sea are also controlled by river discharge, precipitation, atmospheric circulation, and basin-wide water balance. (Azizpour & Ghaffari, 2022) similarly emphasized that Caspian Sea-level variations result from interacting hydrological and climatic processes, particularly evaporation, Volga River discharge, and large-scale atmospheric oscillations. Therefore, the reduction observed in 2022 should not be attributed exclusively to the preceding thermal peak. Instead, the results support a broader interpretation in which regional warming operates alongside multiple hydrological drivers.

The thermal consequences of shoreline retreat are particularly important. When water recedes, previously inundated surfaces become exposed. These areas often have sparse vegetation, limited soil moisture, and reduced evaporative cooling. They can consequently absorb and store more solar energy than the former water surface and may develop into persistent coastal thermal hotspots. Moreover, an increase in the distance between urban areas and the shoreline could diminish the local cooling influence of marine air circulation. This interpretation is consistent with studies showing that vegetation loss, built-up expansion, and changes in surface properties substantially affect LST and SUHI intensity (Fu & Weng, 2016; Wong et al., 2021).

Nevertheless, the observed association should be interpreted cautiously. The present analysis identifies a spatiotemporal correspondence between changes in mapped water extent and surface temperature, but it does not independently establish a direct causal effect of shoreline retreat on urban warming. Air temperature, humidity, wind direction, vegetation dynamics, soil moisture, urban expansion, and anthropogenic heat emissions may simultaneously influence LST. A stronger causal assessment would require multivariable modeling, explicit controls for meteorological conditions and land-cover change, and comparison of newly exposed coastal surfaces with stable reference areas.

Substantial differences were observed among the three coastal provinces. Golestan consistently exhibited higher temperatures than Mazandaran and Gilan, indicating a clear east–west thermal gradient along the southern Caspian coast. This contrast can be explained partly by Golestan's drier climate, proximity to the semi-arid landscapes east of the Caspian Sea, lower vegetation density, and potentially greater exposure to shoreline retreat. By comparison, the denser vegetation and higher humidity of Gilan and Mazandaran provide stronger evapotranspirative cooling. Similar climate-dependent differences in surface urban heat island behavior across Iranian cities were reported by (Karimi Firozjaei et al., 2025), who showed that the thermal effects of urban growth vary considerably among humid, semi-arid, and arid environments.

Urbanization further complicates the regional thermal response. The expansion of impervious surfaces, increasing building density, vegetation fragmentation, traffic, and energy consumption can alter the surface-energy balance and reinforce heat accumulation. Consequently, the thermal patterns observed around Rasht, Sari, and Gorgan cannot be explained solely by changes in the Caspian Sea. The findings instead point to a compound process in which coastal hydrological change interacts with urban growth and background climatic conditions. This interaction is especially concerning in Golestan, where climatic dryness and urban development may amplify the thermal effects of newly exposed coastal land.

The comparison between Landsat-derived LST and NASA POWER 2-m air temperature showed strong temporal agreement, with coefficients of determination of 0.8376, 0.8699, and 0.8830 for Rasht, Sari, and Gorgan, respectively. These results support the temporal consistency of the satellite-derived temperature patterns. However, they should not be interpreted as direct validation of LST because surface temperature and near-surface air temperature are physically distinct variables. Future studies should preferably validate satellite-derived LST using ground-based radiometric measurements or another independent LST product acquired at comparable times.

Several additional limitations should be acknowledged. MNDWI measures changes in mapped surface-water extent rather than the elevation of the sea surface; therefore, the results describe shoreline and water-area dynamics, not direct measurements of sea level. The classification is also sensitive to image acquisition dates, cloud contamination, water turbidity, shallow water, wet soil, and the selected MNDWI threshold. Furthermore, annual or seasonal composites may conceal short-term thermal variability and extreme events. These limitations should be addressed through tide-gauge or altimetry data, consistent seasonal image selection, threshold-sensitivity analysis, and higher-resolution observations.

Overall, the study demonstrates that Caspian Sea retreat may represent an emerging component of thermal risk along the northern coast of Iran. The exposure of barren coastal surfaces, possible weakening of water-related cooling, and continued expansion of urban areas may jointly intensify future surface warming. Coastal adaptation should therefore extend beyond conventional urban heat mitigation. It should include the protection and ecological restoration of newly exposed land, preservation of coastal ventilation corridors, expansion of native vegetation, restriction of uncontrolled construction near the changing shoreline, and wider use of cool and permeable urban surfaces. Continued satellite monitoring, combined with hydrological observations and multivariable climate modeling, will be essential for distinguishing the contribution of shoreline retreat from other drivers and for guiding climate-resilient planning across the rapidly changing Caspian coastal zone.

Data statement

Data is available.

Conflict of Interest

There is no conflict of interest regarding the publication of this paper.

6. References

Azizpour, J., & Ghaffari, P. (2022). *Low-frequency Sea level changes in the Caspian Sea: long-term and seasonal trends*. https://doi.org/10.21203/rs.3.rs-1845231/v1

Beyraghdar Kashkooli, O., Ghadami, M., Amini, M., & Modarres, R. (2019). Spatiotemporal variation of the southern Caspian Sea surface temperature during 1982–2016. *Journal of Marine Systems*, *193*, 126–136. https://doi.org/10.1016/j.jmarsys.2019.02.006

Caspian Sea Studies, & Center, R. (2025). *Analysis of thermal regulation and shoreline retreat in Northern Iran*.

Dwivedi, A., & Soni, R. (2024). Impacts of urban heat island effect on critical urban infrastructure: a review of studies published between 2012 and 2022. *Environmental Reviews*, *32*(4), 457–469. https://doi.org/10.1139/er-2023-0108

Feinberg, A. (2023). Urbanization Heat Flux Modeling Confirms It Is a Likely Cause of Significant Global Warming: Urbanization Mitigation Requirements. *Land*, *12*(6), 1222. https://doi.org/10.3390/land12061222

Fu, P., & Weng, Q. (2016). A time series analysis of urbanization induced land use and land cover change and its impact on land surface temperature with Landsat imagery. *Remote Sensing of Environment*, *175*, 205–214. https://doi.org/10.1016/j.rse.2015.12.040

Ghanghermeh, A., Roshan, G., Asadi, K., & Attia, S. (2024). Spatiotemporal Analysis of Urban Heat Islands and Vegetation Cover Using Emerging Hotspot Analysis in a Humid Subtropical Climate. *Atmosphere*, *15*(2), 161. https://doi.org/10.3390/atmos15020161

Gorelick, N., Hancher, M., Dixon, M., Ilyushchenko, S., Thau, D., & Moore, R. (2017). Google Earth Engine: Planetary-scale geospatial analysis for everyone. *Remote Sensing of Environment*, *202*, 18–27. https://doi.org/10.1016/j.rse.2017.06.031

Hedeya, Y., Merabtine, A., & Maref, W. (2025). Evaluating the Urban Heat Island Effect in Montreal: Urban Density, Vegetation, Demographic, and Thermal Landscape Analysis. *Buildings*, *15*(9), 1562. https://doi.org/10.3390/buildings15091562

Huang, Q., & Lu, Y. (2018). Urban heat island research from 1991 to 2015: a bibliometric analysis. *Theoretical and Applied Climatology*, *131*(3–4), 1055–1067. https://doi.org/10.1007/s00704-016-2025-1

Karimi Firozjaei, M., Mahmoodi, H., & Jokar Arsanjani, J. (2025). Daytime Surface Urban Heat Island Variation in Response to Future Urban Expansion: An Assessment of Different Climate Regimes. *Remote Sensing*, *17*(10), 1730. https://doi.org/10.3390/rs17101730

Liang, B., Shi, G., Wu, H., Qu, S., Wang, M., & Sun, Z. (2026). Analysis of urban resilience assessment and spatiotemporal patterns in coastal cities under sea-level rise. *Scientific Reports*, *16*(1), 6119. https://doi.org/10.1038/s41598-026-37425-x

Macintyre, H. L., Heaviside, C., Cai, X., & Phalkey, R. (2021). Comparing temperature-related mortality impacts of cool roofs in winter and summer in a highly urbanized European region for present and future climate. *Environment International*, *154*, 106606. https://doi.org/10.1016/j.envint.2021.106606

Nadeem, M., & others. (2023). Urban Heat Island as a significant environmental consequence of urbanization. *Computers*, *12*(9).

NASA POWER Project. (2024). *Prediction of Worldwide Energy Resources*. https://power.larc.nasa.gov/

Ojerinde, G. E., Ochai, T., & Agbelade, A. D. (2026). Monitoring urban thermal stress and forest resilience for climate change mitigation in megacities, Northwest, Nigeria. *Discover Geoscience*, *4*(1), 73. https://doi.org/10.1007/s44288-026-00462-0

Omidighalehmohammadi, Z., Morovati, M., Karami, P., & Parvar, Z. (2026). Spatiotemporal modeling of urban green space connectivity and landscape structure for climate adaptation in Tehran, Iran. *PLOS One*, *21*(4), e0341276. https://doi.org/10.1371/journal.pone.0341276

Sayah, M. Al, Soto, D., Nedjai, R., Selouane, K., Ziv, N., & Sohouenou, P. (2023). On the use of remote sensing and modeling techniques for urban heat detection, an operational study. *2023 Joint Urban Remote Sensing Event (JURSE)*, 1–5. https://doi.org/10.1109/JURSE57346.2023.10144167

U.S. Geological Survey. (2024). *Landsat 8-9 Collection 2 Level-2 Science Product Guide*.

Weng, Q., Firozjaei, M. K., Sedighi, A., Kiavarz, M., & Alavipanah, S. K. (2019). Statistical analysis of surface urban heat island intensity variations: A case study of Babol city, Iran. *GIScience & Remote Sensing*, *56*(4), 576–604. https://doi.org/10.1080/15481603.2018.1548080

Wong, N. H., Tan, C. L., Kolokotsa, D. D., & Takebayashi, H. (2021). Greenery as a mitigation and adaptation strategy to urban heat. *Nature Reviews Earth & Environment*, *2*(3), 166–181. https://doi.org/10.1038/s43017-020-00129-5

Xu, H. (2006). Modification of normalised difference water index (NDWI) to enhance open water features in remotely sensed imagery. *International Journal of Remote Sensing*, *27*(14), 3025–3033. https://doi.org/10.1080/01431160600589179

Zhao, E., Liu, X., & Wang, Y. (2026). Local Climate Zone-Based Analysis of Urban Heat Island Influencing Factors in Coastal Cities Across Multiple Climate Zones. *Remote Sensing*, *18*(5), 762. https://doi.org/10.3390/rs18050762